Oscillation Risks of Grid-Following and Grid-Forming Inverter-Based Resources in Series-Compensated Networks

Ratik Mittal, *Member, IEEE*, Zhixin Miao, *Senior Member, IEEE*, Lingling Fan, *Fellow, IEEE*, Deepak Ramasubramanian, *Senior Member, IEEE*

***Abstract*—This paper investigates the dynamic behavior of a grid-connected inverter-based resource (IBR) when connected radially to a series compensated line. Potential interactions between the series compensation and the IBR have been identified for both types: grid-following (GFL) or grid-forming (GFM). The study begins with electromagnetic transient (EMT) simulations to demonstrate stability issues. Subsequently, nonlinear analytical models are formulated in the dq frame, validated against the EMT simulation, and leveraged to assess eigenvalues and participation factors. Influencing factors of the dominant oscillation modes have been identified. The analysis results show that series compensation may make a mode associated with the synchronization unit unstable. Furthermore, customized feedback systems are built for the synchronizing loop. Series compensation can increase the sensitivity of the voltage phase angle towards the synchronizing angle, and introduce phase lag in the real power response towards the synchronizing angle. These factors may cause interactions with the phase-locked loop in GFL-IBR systems and with power-based synchronization in GFM-IBR systems, potentially leading to instability.**

***Index Terms*—Series Compensation, grid following, grid forming, stability, inverter-based resources.**

I. Introduction

SERIES compensation in power grids expands the system's power flow limit and transient stability. While this approach proves economically beneficial, introducing series capacitors brings forth challenges, notably subsynchronous resonances (SSR). A pivotal case in the 1970s at the Mohave generating stations highlighted the connection between the LC resonance mode of transmission lines, the induction generator effect (IGE) of synchronous generators, and rotor shaft oscillation modes, resulting in sustained oscillations and shaft failures [1].

There has been a paradigm shift in the evolving landscape of power grids, integrating IBRs such as type-3 wind turbines, type-4 wind turbines, and solar photovoltaic (PV) systems. However, the increased penetration of IBR sources has introduced unwanted dynamics, including weak grid oscillations and series capacitor related oscillations. The task force paper by the IEEE Power & Energy Society IBR subsynchronous oscillation (SSO) task force [2] provides a survey of 19 real-world SSO events associated with IBRs due to either weak grid interconnection or radial interconnection with series capacitors. A recently published article [3] reviews operational challenges in the IBR interfaced grid and also recommends the examination of series compensation conditions.

Over the years, the root cause of SSO in type-3 wind farms radially connected to series compensated networks has been extensively investigated in the literature [4]–[9]. For instance, [4], [5] have shown that IGE, instead of torsional interactions is the main contributor to SSO due to the negative equivalent rotor resistance of a doubly-fed induction generator in the subsynchronous frequency region, and converter current control exacerbates the effect. More recently, [9] shows that phase-locked-loop (PLL) dynamics can worsen SSO stability.

While the interactions of series capacitor and a type-3 wind farm have been thoroughly investigated in the literature, there exists few literature investigating potential interactions of series capacitors with grid-connected converters popularly adopted in type-4 wind farms, solar PV farms, and battery energy storage systems.

A. Related literature

Back in 2012, with type-3 wind farms already being identified as vulnerable to interactions with series capacitors, a paper from Siemens [10] suggests that type-4 wind farms are immune to series capacitor SSOs based on electromagnetic transient (EMT) simulation results. In the testbed presented in [10], the interconnected grid is assumed to be very strong. In 2019, potential risks of series capacitors to type-4 wind farms were reported in [11]. Authors of [11] adopted frequency-domain admittance-based approach to investigate stability issues in a type-4 wind farm radially connected to a series compensated network. Non-passivity of the type-4 wind farm's admittance in the subsynchronous frequency range is found to contribute to oscillatory instability.

Reference [11] has pointed out instability and attributed instability to inverter admittance being non-passive. On the other hand, non-passivity alone cannot be used to explain why a series compensated network introduces instability, while a non-compensated network does not. Additionally, characteristics of such oscillations have not been analyzed. For example, in type-3 wind farms, an increased compensation level leads to higher oscillation frequency in the phase current and voltage. How does compensation level influence oscillations in type-4 wind farms?

This project is supported in part by U.S. Department of Energy Solar Energy Technologies Office through Grant DE-EE0011474 and EPRI grant 10017639. R. Mittal is with Quanta Technology. Z. Miao, and L. Fan are with the Department of Electrical Engineering, University of South Florida, Tampa, FL, 33620. D. Ramasubramanian is with EPRI. e-mail: linglingfan@usf.edu.

This question has been answered in [12], which provides more granular-level analysis results. The authors particularly pointed out that PLLs may interact with series compensation and cause oscillations. Additionally, the oscillation frequency is associated with the PLL bandwidth, instead of series compensation level. In another word, the series compensation can push the PLL mode to instability. In short, [12] has clearly pointed out the potential interactions of series compensation with the synchronizing unit in a GFL-IBR.

With a paradigm shift in the current power grid, more and more grid-forming IBRs are being integrated. Grid-forming controls (GFM) are recommended by grid reliability authority to provide frequency and voltage support [13]. This control is very different from the conventional grid-following control (GFL). While the GFL control has a PLL acting as the synchronizing unit, the GFM control has power-based synchronization scheme. Will series compensation interacts with GFM-IBRs? Since 2020, a few research papers have initiated investigation. In [14], [15], a virtual synchronous generator (VSG)-based grid-forming IBR is shown to interact with the interconnected series compensated line and create subsynchronous oscillations. The authors have used the impedance-based method for stability analysis. On the other hand, the impedance-based method can only tell stability vs. instability, but cannot provide a more granular root cause analysis.

B. Goals

This paper aims to fill the gaps and address how series compensation may interact with IBRs by providing thorough analysis and validation. In the work, we compare the behavior of GFL-IBRs and GFM-IBRs when they are radially connected to a series compensated network or a non-compensated work. The analysis and validation are conducted in three steps. First, we identify the stability issue with the help of EMT simulations. Second, we develop nonlinear state-space models to perform in-depth analysis. Tools like eigenvalues and participation factors are used to understand the root cause of the stability issues. Although the primary focus is identifying stability issues in GFM-based IBRs, we also revisit GFL-IBRs and provide more detailed explanations. The analysis shows that similar to GFL-IBRs, GFM-IBRs are also prone to oscillatory behavior due to series compensation. Third, we examine the feedback systems associated with the synchronizing angle for the GFL interconnected system and the GFM interconnected system and compare how series compensation influences the subsystems. The comparison and analysis are conducted in the frequency domain. The research results shed insights on series compensation's effect towards various subsystems.

C. Contributions

Our contributions are three-fold:

- Potential stability issues due to the interactions of series compensation and the synchronizing units in IBRs have been quantitatively analyzed by use of analytical model building and eigenvalue-based analysis. This research clearly shows that series compensation, while reducing equivalent grid impedance at the nominal frequency, can make an IBR-integrated system unstable and subject to oscillations.
- This paper further reveals that the frequency-domain response between the IBR's voltage phase angle vs. the synchronizing angle is similar as a high-pass filter with delay, while the frequency-domain response between the IBR's power vs. the synchronizing angle is similar as a low-pass filter with delay. Series compensation increases the gain of the high-pass filter and introduces more phase lag to the low-pass filter, thereby jeopardizing stability.
- In the modeling perspective, the paper contributes to not only standard dq-frame state-space modeling for IBR integrated systems, but also subsystem model extraction for block diagram formulation. The latter facilitates in-depth analysis and insight revealing carried out in the frequency domain.

D. Structure

The rest of the paper is structured as follows. Section II presents the system topology, the control structure for GFM and GFL IBRs, and the EMT simulation results demonstrating stability issues caused by series compensation. Section III presents the dq-domain analytical model and presents the eigenvalue analysis, participation factors. Section IV presents block-diagram based frequency-domain analysis. Section V discusses the performance of alternative control structures, and Section VI concludes this paper.

II. System Topology

The topology is presented in Fig. 1. The system consists of a three-phase DC-AC inverter connected to the power grid via a parallel combination of transmission lines represented by R_g, L_g, and C_g, where C_g is the series compensation. A choke filter is connected between the terminals of the inverter. The choke filter is represented by R_f, L_f and C_f. A constant DC voltage source supplies the inverter, and the AC grid is modeled as a constant voltage source (infinite bus). Furthermore, i_c is the converter current, v_{PCC} is the PCC bus voltage, and i_g is the grid current. In this paper, two testbeds are considered. Testbed-1 has an IBR system operating in the GFL mode with a PLL as the synchronizing unit, and testbed-2 has an IBR operating in the GFM mode with a power-based synchronization unit.

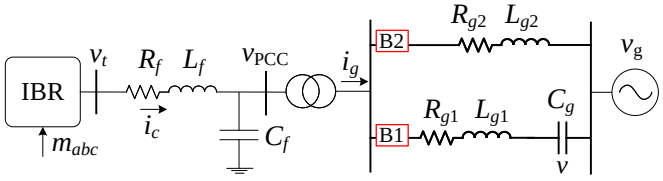

Fig. 1: System topology for a grid-connected IBR power plant.

TABLE I: Circuit Parameters used for testbed-1 and testbed-2.

Description	Parameter	Value	Bandwidth
Power Base	S_b	100 MVA	
Voltage Base	V_b	575 V	
Nominal Frequency	ω_0	$2\pi 60$ rad/s	
Grid Voltage	V_g	1 pu	
Choke Filter	X_f	0.15 pu	
	R_f	0.003 pu	
	B_c	0.25 pu	
Line Inductance	X_{g1}, X_{g2}	vary	
Line Resistor	R_{g1}, R_{g2}	$0.1X_{g1}$, $0.1X_{g2}$	
Control Parameters for GFL IBR			
Inner current	k_{ip}, k_{ii}	0.3, 5	114 Hz
P control	k_{Pp}, k_{Pi}	0.25, 25	4 Hz
V_{PCC}	k_{Vp}, k_{Vi}	0.2, 20	SCR dependent
PLL	$k_{p\text{PLL}}$, $k_{i\text{PLL}}$	150, 10000	33 Hz
		Resonance point	15 Hz
Control Parameters for GFM IBR			
Inner current	k_{ip}, k_{ii}	0.3, 5	114 Hz
v_d control	k_{Pp}, k_{Pi}	0.5, 20	SCR dependent
v_q control	k_{Vp}, k_{Vi}	0.5, 20	SCR dependent
P-f droop	R	0.05	

A. Control Structure

1) GFL: Testbed-1 has the IBR operating in the GFL mode. The inner loop is the current control loop in a dq frame, and the outer loop is real power P and PCC bus voltage magnitude $|V_{\text{PCC}}|$ control. The real power control generates $i_{d\text{ref}}$ for the d-axis current control loop and $|V_{\text{PCC}}|$ generates $i_{q\text{ref}}$ for the q-axis current control loop. A PLL is used to measure the PCC bus angle θ_{PCC} and PLL's output angle θ is used for synchronization. The dq converter voltage references generated by the inner control is converted to the abc reference using the PLL's angle θ. This control structure has been used and validated in computer simulation and hardware experiments, e.g., [16], [17].

2) GFM: In Testbed-2, the IBR is operating the in GFM mode. The control structure is adapted from the works of [16], [18]. Most recently, this control structure has been prototyped in hardware and tested in a hardware testbed [19]. The inner loop and the q-axis outer control are similar as those in testbed-1. The synchronizing angle is generated by the $P-f$ droop and the objective of the d-axis outer control is to have the PCC bus voltage space vector aligned with the synchronizing frame. The control enforces the PCC voltage's projection on the q-axis of the synchronizing frame v_q to be 0. This v_q control generates $i_{d\text{ref}}$ for the d-axis inner current control. The $P-f$ droop regulates the PCC bus's real power and provides the synchronizing angle θ. Here, R is the droop gain defining the per unit change in frequency for one per unit change in power. The control structure for the two IBRs is presented in Fig. 2. Table I presents the parameters used for testbed-1 and testbed-2.

For the GFL IBRs, initial analysis is provided for different PLLs. The four examined PLLs are:

1) PLL-1 ($k_{p\text{PLL}}, k_{i\text{PLL}}$): (60, 1400) no low-pass filter (LPF). It has a bandwidth of 13 Hz, with a peak magnitude occurring at 5 Hz (resonant frequency).
2) PLL-2 ($k_{p\text{PLL}}, k_{i\text{PLL}}$): (180, 3200) with a first-order LPF. The bandwidth is 35 Hz, and the resonant frequency is 21 Hz.
3) PLL-3 ($k_{p\text{PLL}}, k_{i\text{PLL}}$): (150, 10000), featuring a bandwidth of 33 Hz and a resonant frequency of 15 Hz.
4) PLL-4 ($k_{p\text{PLL}}, k_{i\text{PLL}}$): (150, 2000) with a second-order LPF. It has a bandwidth of 30 Hz, with a peak magnitude occurring at 20 Hz.

The LPF is designed with a 25 Hz natural frequency and a 0.707 damping ratio. Fig. 3a shows the Bode diagram of four PLLs, where the resonant frequency corresponds to the peak amplitude. Among them, PLL-3 shows a resonance peak at 15 Hz while PLL-4 exhibits a peak at 20 Hz. The time-domain results are shown in Fig. 3b. PLL-4 leads to the worst stability when the GFL-IBR is radially connected to an RLC network (0.38 pu total reactance and 62% compensation level), while PLL-1 remains stable. PLL-2 and PLL-3 perform similarly, with 15 Hz oscillations. Notably, despite PLL-2's higher bandwidth, it offers better stability than PLL-4. PLL-3 will be assumed for the EMT studies in the following subsection.

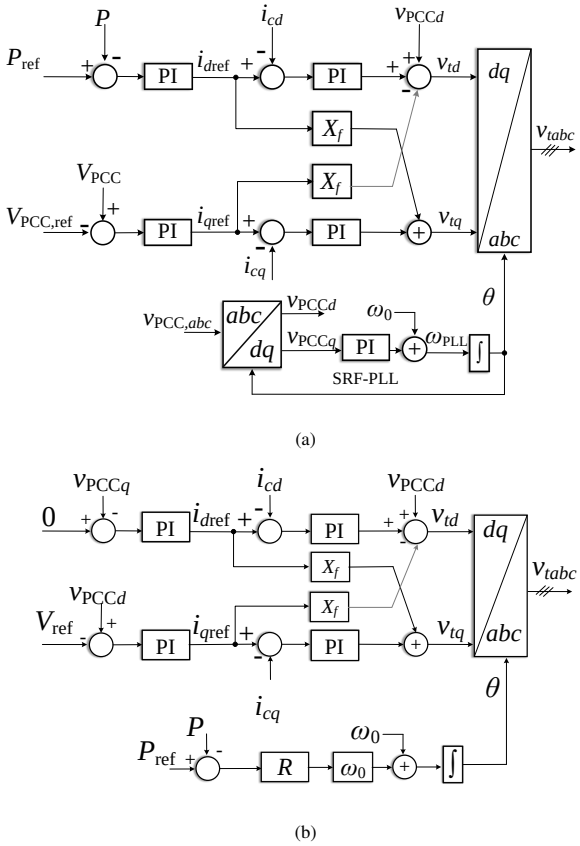

Fig. 2: Control Structure. (a) GFL. (b) GFM.

B. EMT Simulation Results

EMT simulations are conducted using MATLAB/Simscape Electrical Specialized Power Systems. The two testbeds are subjected to a line tripping event at $t = 30$ s. Two types of line tripping events are examined. In case 1 (breaker B2 opens), the RL circuit is tripped leaving the IBR radially connected to the RLC circuit. In case 2 (breaker B1 open1), the RLC circuit is tripped leaving the IBR radially connected to the RL

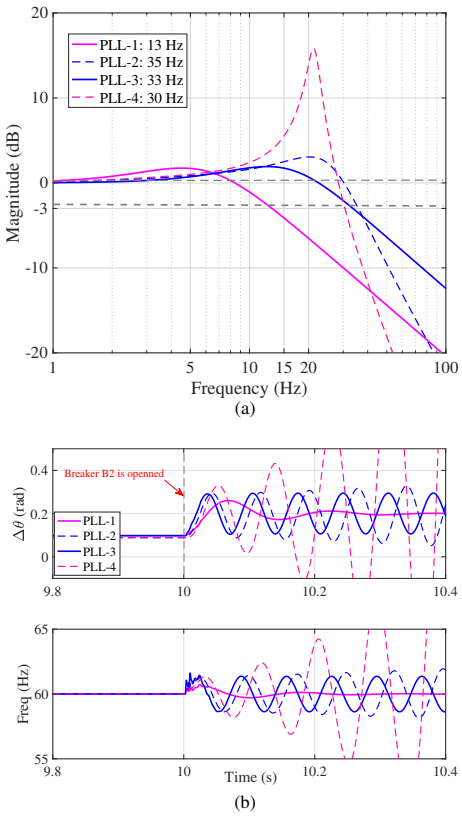

Fig. 3: (a) Bode diagram of the transfer function of different SRF-PLLs. GFL. (b) Time-domain responses of the PLL angle $\Delta\theta$ and Frequency (Hz) for different PLLs when the GFL IBR is radially connected to RLC network with effective impedance of 0.38 pu.

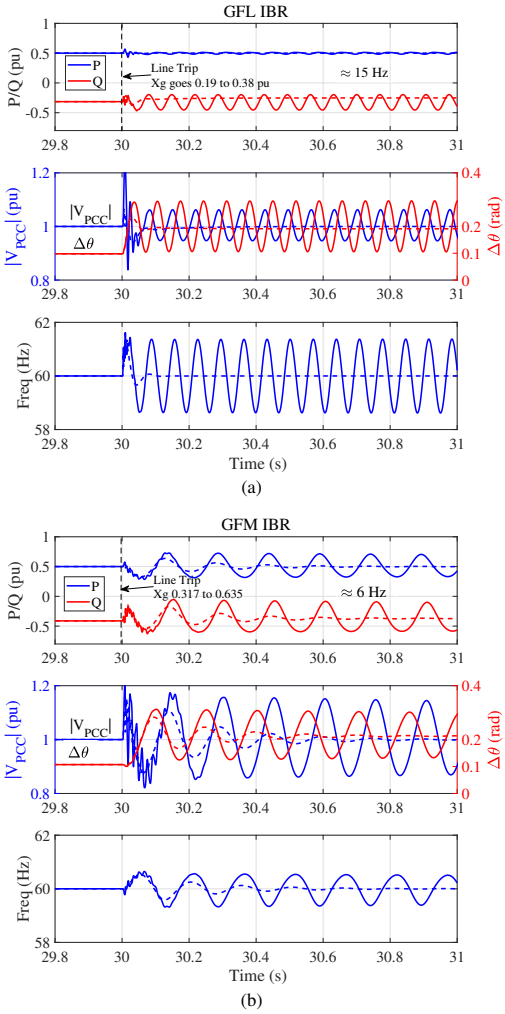

Fig. 4: Time-domain responses for the real power P, Q, $|V_{\text{PCC}}|$, $\Delta\theta$,and frequency (Hz). Solid lines: with series compensation. Dashed lines: without series compensation. The line tripping occurs at $t = 30$ s. (a) GFL (b) GFM.

circuit. Furthermore, the RL circuit and the RLC circuit have the same effective grid reactance. The operating conditions are as follows: $P_{\text{ref}} = 0.5$ pu, and $V_{\text{PCC,ref}} = 1$ pu. The line parameters for the testbeds are shown in Table II.

TABLE II: Line parameters for the testbeds in two cases.

	RLC circuit	RL circuit
testbed-1	$X_{g1} = 1$ pu, $X_{Cg} = 0.62$ pu	$X_{g2} = 0.38$ pu
testbed-2	$X_{g1} = 1$ pu, $X_{Cg} = 0.365$ pu	$X_{g2} = 0.635$ pu

The time-domain simulation results are shown in Fig. 4 for the two specified cases. For testbed-1 with a GFL-IBR, the initial grid reactance is 0.19 pu. When the line is tripped at $t = 30$ s, for case 1 (RLC), the system is connected to a series compensated network ($K = 62\%$) and the total grid reactance of 0.38 pu. K represents the level of series compensation. Similarly, for case 2, the grid reactance changes from 0.19 pu to 0.38 pu. On observing results presented in Fig. 4a, we can see that for similar operating conditions, when the GFL-IBR is connected to the RLC network, undamped 15 Hz oscillations appear. When the GFL-IBR is connected to RL network, the system is stable. Hence, it can be said that the series compensation introduces unwanted stability issues.

Similarly, the same can be said on observing results presented in Fig. 4b for testbed-2 of the GFM-IBR. For case 1, when the system is connected to the series compensated network (RLC, $K = 36.5\%$), the system undergoes an undamped oscillation of around 6 Hz. However, when connected to the RL network, a line tripping event (total grid impedance changes from 0.317 pu to 0.635 pu), the system is stable and the 6-Hz oscillations can be quickly damped out. Hence, the EMT simulation results demonstrate the interactions of a series compensated line with an IBR in either GFL or GFM modes.

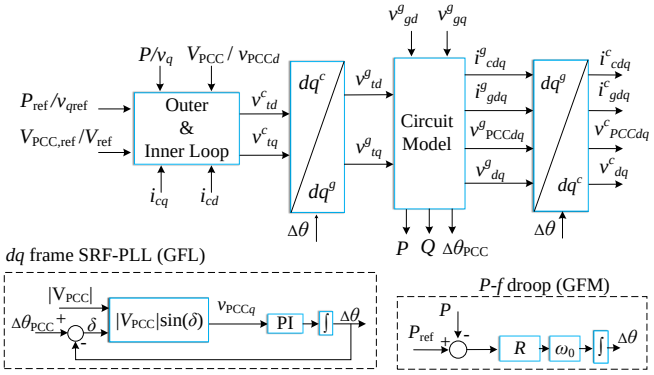

Fig. 5: The dq frame analytical model for GFL and GFM IBR.

III. Analytical Modeling and Analysis Results

In this section, we examine the influencing factors of the observed 15-Hz and 6-Hz oscillations in the two testbeds. While EMT simulation results show that series capacitor is the main influencer, we are not able to obtain further insights regarding how inverter control blocks contribute to the oscillations. The EMT simulation results of testbed-1show that reactive power measurements have more obvious oscillations compared to the real power measurements, implicating q-axis control and PLL may play a role. On the other hand, to have a clear view of the influencing factors, eigenvalue-based analysis is necessary. To have linear time invariant (LTI) model through Jacobian linearization, we will build a nonlinear analytical model representing the IBR radially connected to an RLC circuit. The model has all its state variables constant at steady state to ensure Jacobian linearization.

A. Analytical Model

The analytical model is developed in the dq domain. The system presented in Fig. 1 is modeled with four main blocks: a synchronization unit (PLL or P-f droop), inner and outer control, circuit dynamics, and frame conversion, as shown in Fig. 5. It is noted that, while the signals at the circuit level are based on the grid frame (superscript **g**, rotating at the nominal frequency of ω_0), the signals associated with the control structure are based on the frame or angle provided by the synchronization unit.

The state variables for both testbeds are described as follows: the grid-frame variables associated with circuit dynamics, including the converter current i^g_{cdq}, the PCC bus voltage $v^g_{\text{PCC}dq}$, the grid current i^g_{gdq}, and the series capacitor voltage v^g_{dq} (circuit dynamics), synchronizing-frame states representing the outer loop PI controllers x_1 (d-axis) and x_2 (q-axis) and inner current controls x_3 and x_4. In the GFL-IBR, the PLL incorporates two state variables: $\Delta\omega$ (associated with PI controller) and $\Delta\theta$. Conversely, in the GFM-IBR, the synchronization unit has one state variable $\Delta\theta$. Consequently, the GFL-IBR testbed comprises 14 state variables, while the GFM IBR system consists of 13 state variables.

1) Circuit Dynamics: The analytical model of the circuit dynamics is developed in the grid dq frame that rotates at a speed of ω_0. The 8th-order differential equations for the series RLC circuit and the shunt capacitor dynamics are not presented. Interested readers may refer to our previous papers (e.g., [9]) on the equations. This block has v^g_{td} and v^g_{tq} (the dq components of the converter terminal voltage v_t) and the grid voltage v^g_{gd}, v^g_{gq} as input and outputs the converter current, PCC bus voltage, real and reactive power.

Similarly, the modeling block for the RL circuit is also developed.

2) SRF-PLL: The synchronization unit in testbed-1's GFL-IBR is PLL. For this paper, we have adopted a second-order PLL. The dq frame analytical model of the PLL is adapted from the work presented in [20].

3) Frame conversion: As previously mentioned, the control system operates in a distinct reference frame (angle θ) provided by the synchronization unit, which is a PLL for testbed-1 and a P–f droop for testbed-2. The converter control regulates the dq components of converter current i_c and the voltage at the PCC bus v_{PCC} in the control frame. Due to the different reference frames adopted for the circuit model and the control, appropriate frame conversion is essential for accurate modeling.

The relationship between the grid frame and the control frame can be found by relating the space vector of current or voltage with its grid frame-based and control frame based vectors. For example, the PCC bus voltage's space vector $\vec{v}_{\text{PCC}}$ can be related to the grid-frame variables and the control-frame variables as follows:

$$\begin{aligned}\vec{v}_{\text{PCC}} &= (v_{\text{PCC}d} + j\, v_{\text{PCC}q})e^{j\theta} = (v^g_{\text{PCC}d} + j\, v^g_{\text{PCC}q})\, e^{j\omega_0 t} \\ \Longrightarrow &(v_{\text{PCC}d} + j\, v_{\text{PCC}q})e^{\Delta\theta} = v^g_{\text{PCC}d} + j\, v^g_{\text{PCC}q}, \end{aligned} \tag{1}$$

where $\Delta\theta = \theta - \omega_0 t$. From (1), it can be seen that signals in the grid frame can be transformed to the synchronization frame and vice-versa. The complete analytical model is presented in Fig. 5.

B. Eigenvalue and Participation Factor Analysis

This subsection presents linear system analysis results based on the developed analytical models. We examine the impact of compensation levels (case study 1) and the effects of grid impedance under non-compensated condition (case study 2) for both testbeds.Table III documents the four types of scenarios.

TABLE III: Case studies examined for eigenvalue analysis.

	case study 1	case study 2
GFL	with the RLC circuit only	with the RL circuit only
GFM	with the RLC circuit only	with the RL circuit only

1) Case Study 1: Effect of Series Compensation Level: The eigenvalue loci with varying levels of series compensation (K) are presented in Fig. 6. Here, the compensation level varies with a step size of 1%. The eigenvalue loci analysis reveals two modes affected by changes in the compensation level. Mode 1 is situated around the 60 Hz frequency, while Mode 2 is found at 15 Hz for the GFL-IBR and 6 Hz for the GFM-IBR. Mode 1 consistently remains in the Left-Hand Plane (LHP), indicating stability. In contrast, Mode 2 shifts to the Right-Hand Plane (RHP) as the compensation level increases, signifying instability. For the GFL-IBR, the system loses stability when the level of series compensation is more than 66%, whereas in the case of GFM-IBR, the limit is 40%.

These findings are consistent with the EMT simulation results. When an IBR is directly connected to a series-compensated line, it exhibits undamped oscillations. Specifically, the GFL-IBR oscillates at 15 Hz, while the GFM-IBR oscillates at 6 Hz.

Participation factors (PFs) are numerical measures that indicate the degree to which individual state variables contribute to a specific mode of the system. For Case Study 1, PFs are computed for two modes, Mode 1 and Mode 2, at $K = 66\%$ for the GFL-IBR and $K = 40\%$ for the GFM-IBR. The PFs are listed in Table IV, and Table V. The computed PFs reveal

that Mode 1 is closely associated with the series capacitor. Conversely, for Mode 2, the primary contribution stems from state variables linked to the synchronization unit. Specifically, in the GFL-IBR, the PLL plays a significant role, while in the GFM-IBR, the synchronizing units including the P–f droop-based angle generation and the d-axis outer control to align the PCC bus voltage to the synchronizing frame, influences Mode 2 dynamics.

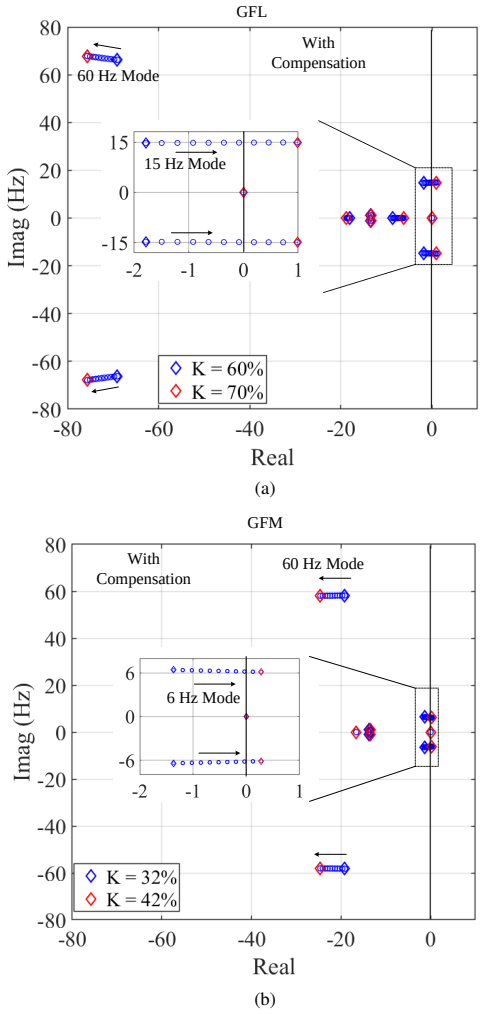

Fig. 6: The eigenvalue loci with increasing series compensation levels with a step size of 1%. (a) GFL (b) GFM.

2) Case Study 2: Grid reactance change: In Case Study 2, we analyze an IBR power plant connected to the grid through the RL circuit. The eigenvalue loci, which vary with grid reactance X_{g2}, are illustrated in Fig. 7. One notable distinction in our findings is the absence of Mode 1 at 60 Hz, previously identified in an RLC circuit, in both testbed-1 and testbed-2 configurations. In testbed-1, the mode at 20 Hz shifts towards right, when the grid strength reduces. The system is stable even for a grid reactance of 1. In testbed 2, the 6-Hz mode resides in the LHP, suggesting a stable system. The eigenvalue loci confirm the knowledge regarding grid strength and IBR [21]: weak grid strength makes a GFL-IBR system less stable while strong grid strength makes the GFM-IBR system less stable.

TABLE IV: Participation Factors of testbed-1 (GFL-IBR) at K = 66%.

	State Variables	Mode 1 60 Hz	Mode 2 15 Hz
Circuit Dynamics	i_{cd}^g	0.0837	0.0049
	i_{cq}^g	0.0102	0.0488
	i_{gd}^g	0.04	0.0018
	i_{gq}^g	0.1979	**0.2676**
	PCC volt $v_{\text{PCC}d}^g$	**0.2438**	0.0062
	PCC volt $v_{\text{PCC}q}^g$	0.0199	0.0128
	series cap v_d^g	**0.2082**	**0.1967**
	series cap v_q^g	**0.4634**	0.0133
PLL	$\Delta\theta$	0.0191	**0.5512**
	$\Delta\omega$	0.003	**0.3217**
Outer Loop	x_1	0.0131	0.0072
	x_2	0.018	0.028
Inner Loop	x_3	0.0041	0.0148
	x_4	0.0007	0.0597

TABLE V: Participation Factors of testbed-2 (GFM-IBR) at K = 40%.

	State Variables	Mode 1 60 Hz	Mode 2 6 Hz
Circuit Dynamics	i_{cd}^g	0.0257	0.025
	i_{cq}^g	0.0023	0.006
	i_{gd}^g	0.0526	0.0117
	i_{gq}^g	0.0443	**0.1056**
	PCC volt $v_{\text{PCC}d}^g$	0.1338	0.0101
	PCC volt $v_{\text{PCC}q}^g$	0.0033	0.0012
	Series cap v_d^g	**0.3002**	0.044
	Series cap v_q^g	**0.4465**	0.0026
Droop	$\Delta\theta$	0.0037	**0.4466**
Outer Loop	x_1	0.008	**0.405**
	x_2	0.008	0.171
Inner Loop	x_3	0.0021	0.0109
	x_4	0.0017	0.1378

On the other hand, the eigenvalue loci plots show that without series compensation, the systems are stable.

Additionally, PFs are computed for Mode 2 at $X_{g2} = 1$ pu for the GFL-IBR and GFM-IBR. The PFs are listed in Table VI. In the case of GFL-IBR, Mode 2 is associated with the PLL state variable and the q-axis grid current. On the other hand, for GFM-IBR, Mode 2 is associated with the droop control and outer loop v_q control. Essentially, Mode 2 is associated with the synchronization unit in an IBR.

Remarks: Comparison of the eigenvalue loci for the testbeds with and without series compensation shows that the LC mode at 60 Hz introduced by the series capacitor pushes the mode in the lower frequency region associated with the synchronization unit to the RHP, causing stability issues.

C. Understanding the 60-Hz mode introduced by series compensation

The previous analytical results show that for an IBR (GFL or GFM) grid integrated system, radial connection with a series capacitor introduces a 60-Hz mode in the dq-frame. This mode does not exist if the IBR is radially connected to an RL circuit. Eigenvalue loci show that when the series compensation level increases, the 60-Hz mode is pushed to the LHP while the mode associated with synchronization is pushed to the RHP.

This mode at 60 Hz is worthy to be investigated. In a type-3 wind farm system, series compensation introduces super- and a sub-synchronous modes (both associated with the LC

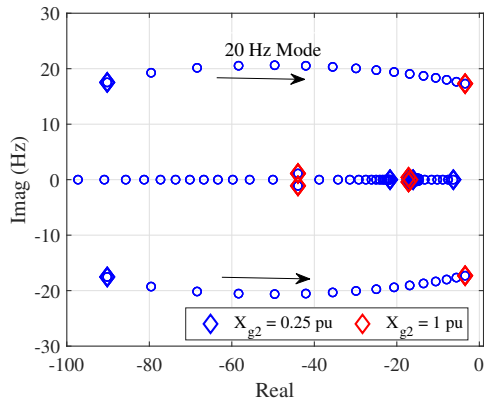

(a)

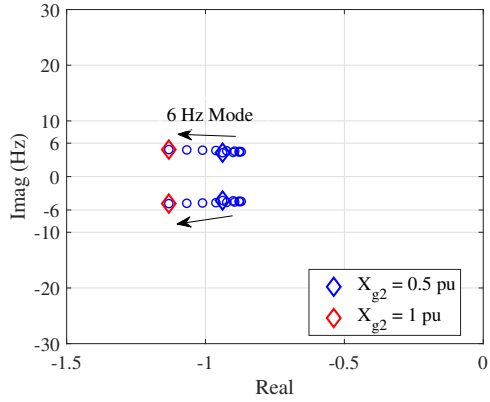

(b)

Fig. 7: The eigenvalue loci with increasing grid reactance (uncompensated network) with a step size of 5%. (a) GFL. (b) GFM.

TABLE VI: Participation Factors of Mode 2 in GFM and GFL IBRs at $X_{g2} = 1$ pu in Case Study 2.

	State Variables	GFL 20 Hz	GFM 6 Hz
Circuit Dynamics	i^g_{cd}	0.0386	0.0259
	i^g_{cq}	0.0659	0.0037
	i^g_{gd}	0.039	0.0079
	i^g_{gq}	**0.3462**	0.0699
	$v^g_{\text{PCC}d}$	0.0897	0.009
	$v^g_{\text{PCC}q}$	0.0192	0.0011
PLL/ Droop	$\Delta\theta$	**0.5083**	**0.5133**
	$\Delta\omega$	0.2694	N/A
Outer Loop	x_1	0.0819	**0.4245**
	x_2	0.1072	0.1259
Inner Loop	x_3	0.0029	0.0118
	x_4	0.0636	0.1123

resonance) [4], [22]. On the other hand, the studied IBR systems in this paper representing solar PVs, type-4 wind farms, and battery energy storage systems (BESS) do not have super- and sub-synchronous modes introduced by series compensation. Instead, a 60-Hz mode is introduced.

The discrepancy is speculated as follows. A type-3 wind farm behaves more like a voltage source (due to the shunt magnetizing inductance of the induction machine). When it is connected to an RLC circuit, an SSR mode is introduced in the static abc frame, which manifests as the super- and sub-synchronous modes. On the other hand, solar PVs, type-4 wind farms, and BESS are more aligned with current sources in the subsynchronous region. When a current source is connected to an RLC circuit, a 60-Hz mode is introduced in the dq-frame voltage.

The speculation is also demonstrated using the following quantitative analysis. Using a voltage-source powered RLC circuit, we can easily see a subsynchronous mode (e.g., a mode at 42 Hz for 50% compensation, when $\frac{1}{\omega_0 C} = 0.5\omega_0 L$ and $\omega_0 = 377$ rad/s) introduced in the phase currents, since

$$\Delta i = \frac{1}{R + Ls + \frac{1}{Cs}} v = \underbrace{\frac{Cs}{LCs^2 + RCs + 1}}_{Y(s)} \Delta v, \tag{2}$$

where $Y(s)$'s magnitude has a resonance peak at the LC resonance frequency of $\omega_{LC} = \frac{1}{\sqrt{LC}}$.

In the dq frame with a rotating speed of ω_0 (377 rad/s), the relationship becomes:

$$\Delta\overline{I} = \frac{1}{R + L(s + j\omega_0) + \frac{1}{C(s+j\omega_0)}} \overline{V}$$
$$\Longrightarrow \begin{bmatrix} \Delta i_d \\ \Delta i_q \end{bmatrix} \begin{bmatrix} Y_d & -Y_q \\ Y_q & Y_d \end{bmatrix} \begin{bmatrix} \Delta v_d \\ \Delta v_q \end{bmatrix} \tag{3}$$

where

$$Y_d = \frac{R + Ls + \frac{s}{C(s^2+\omega_0^2)}}{\left(R + Ls + \frac{s}{C(s^2+\omega_0^2)}\right)^2 + \left(L\omega_0 - \frac{\omega_0}{C(s^2+\omega_0^2)}\right)^2} \tag{4}$$

$$Y_q = -\frac{L\omega_0 - \frac{\omega_0}{C(s^2+\omega_0^2)}}{\left(R + Ls + \frac{s}{C(s^2+\omega_0^2)}\right)^2 + \left(L\omega_0 - \frac{\omega_0}{C(s^2+\omega_0^2)}\right)^2} \tag{5}$$

Y_d and Y_q have two resonance peaks at the $\omega_0 + \omega_{LC}$ and $\omega_0 - \omega_{LC}$. It can be viewed as the subsynchronous mode with oscillation frequency of ω_{LC} becomes two modes: a sub- and a super-synchronous modes. For example, if we observe 42 Hz oscillations in the phase currents, in the dq frame or RMS voltage or current, we expect to see 18 Hz and 102 Hz oscillations. Fig. 8a shows the three admittance $Y(s)$, $Y_d(s)$ and $Y_q(s)$. It can be seen that if a peak appears at 42 Hz in the admittance observed in the static frame, in the dq frame admittances, two peaks appear, one at 18 Hz and the other at 102 Hz.

On the other hand, for a current source powered RLC circuit, the voltage at the PCC bus is dependent on the impedance of the RLC circuit.

$$\Delta v = \underbrace{\left(R + Ls + \frac{1}{Cs}\right)}_{Z(s)} \Delta i. \tag{6}$$

In the dq frame, the expression becomes:

$$\Delta\overline{V} = \left(R + L(s + j\omega_0) + \frac{1}{C(s + j\omega_0)}\right) \Delta\overline{I} \tag{7}$$
$$\Longrightarrow \begin{bmatrix} \Delta v_d \\ \Delta v_q \end{bmatrix} \begin{bmatrix} Z_d & -Z_q \\ Z_q & Z_d \end{bmatrix} \begin{bmatrix} \Delta i_d \\ \Delta i_q \end{bmatrix} \tag{8}$$

where

$$Z_d = R + Ls + \frac{s}{C(s^2 + \omega_0^2)} \tag{9}$$

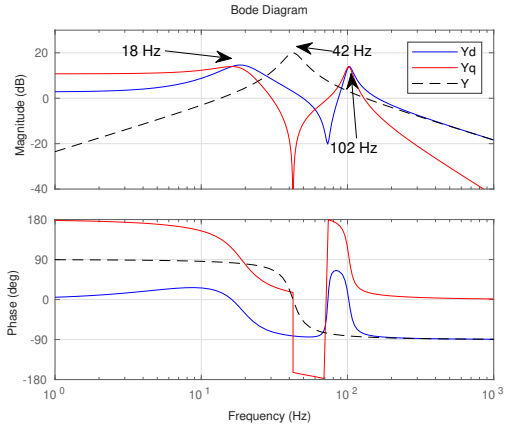

(a)

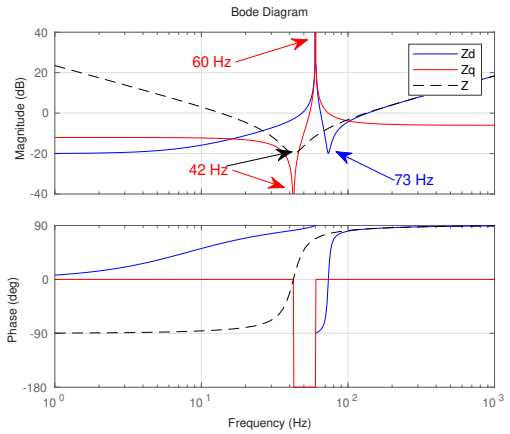

(b)

Fig. 8: (a) Admittances of the RLC circuit. (b) Impedances of the RLC circuit.

$$Z_q = \omega_0 L - \frac{\omega_0}{C(s^2+\omega_0^2)} \tag{10}$$

It can be seen that in the static frame the transfer function of $Z(s)$ has a pole at 0 Hz while in the dq frame the transfer function matrix has two poles of $\pm j\omega_0$ introduced and the frequency of the mode is 60 Hz.

Therefore, the speculation that the 60-Hz pole is introduced because of type-4 wind and solar PV behave as current sources makes sense. Fig. 8b shows the Bode diagrams of the impedance Z observed in the static frame and Z_d and Z_q observed in the dq frame. It can be seen that in both Z_d and Z_q, the resonance peak is at 60 Hz, implicating a mode of 60 Hz.

IV. Block Diagrams and Frequency-Domain Analysis

The developed analytical model can provide further insights into the system by analyzing the frequency domain's open-loop transfer functions (gains). Open-loop gain can provide us with a substantial understanding of the system stability. From the previous results presented in the form of eigenvalues and participation factors, we found that when the system is radially connected to a series compensation network (RLC circuit), the system may lead to instability when the synchronization unit interacts with the RLC circuit. Hence, a feedback system with two blocks will be constructed with the synchronization unit (PLL in testbed-1 and P–f droop in testbed-2) connected to the rest of the system.

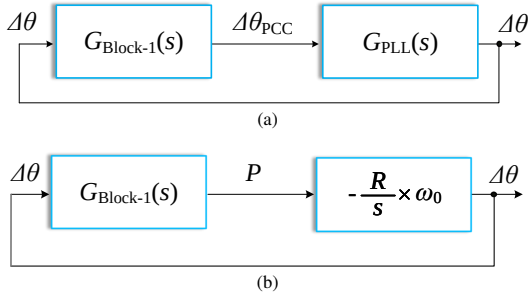

Fig. 9: Feedback system construction: the synchronizing loop. (a) GFL. (b) GFM.

Fig. 9 presents the block diagram representation of the decoupled open-loop system, which enables us to study the interaction of the synchronization unit with the rest of the system. The stability assessment is done by evaluating the gain margin from the magnitude plot of the frequency response at the frequency when phase shift happens from -180° to 180°. Here, "Block-1" represents the transfer function from the synchronizing angle $\Delta\theta$ to the PCC bus voltage angle $\Delta\theta_{\text{PCC}}$ or the real power measurement P. This block can be found from the analytical model by treating the synchronizing angle as a constant and conducting linearization.

The total open-loop transfer functions $G_{\text{OL}}(s)$ for testbed-1 and testbed-2 are given by:

$$\begin{aligned} G_{\text{OL}}(s) &= -G_{\text{Block-1}}(s) \times G_{\text{PLL}}(s), \\ G_{\text{OL}}(s) &= -G_{\text{Block-1}}(s) \times G_{\text{droop}}(s). \end{aligned} \tag{11}$$

The transfer function of the PLL and droop control is given by:

$$\begin{aligned} G_{\text{PLL}}(s) &= \frac{k_{p\text{PLL}}s + k_{i\text{PLL}}}{s^2 + k_{p\text{PLL}}s + k_{i\text{PLL}}} \\ G_{\text{droop}}(s) &= -\frac{R}{s} \times \omega_0 \end{aligned} \tag{12}$$

For GFL-IBR, on observing just the Bode diagram of block-1 in Fig. 10a, we can see that for an RLC network, the gain in the range of 1 Hz to 50 Hz is greater than that of the RL network. For the total open-loop gain, including the PLL, the system is marginally unstable for RLC interconnection and stable for RL interconnection, as shown in Fig. 10b. Since the phase shifting happens at 15 Hz, it is expected to have 15-Hz oscillation mode. This observation aligns with the eigenvalue analysis results in Fig. 6a, showing a 15-Hz mode in the RHP when the compensation level increases.

When the GFL is radially connected to the RL circuit, the phase shifting happens at 20 Hz, implicating a 20-Hz oscillation mode. This again corroborates the eigenvalue loci shown in Fig. 7a, where a 20-Hz oscillation mode moving towards right when the grid strength reduces, without losing stability for 50% of power exporting level.

Furthermore, Fig. 10c presents the effect of different PLLs on the stability of GFL IBR when connected to RLC network

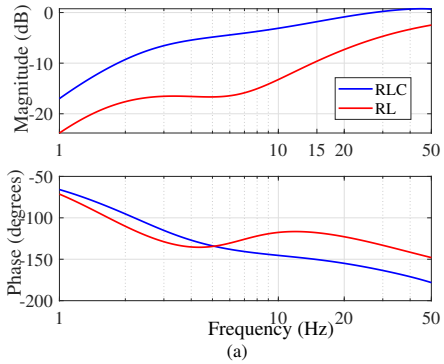

(a)

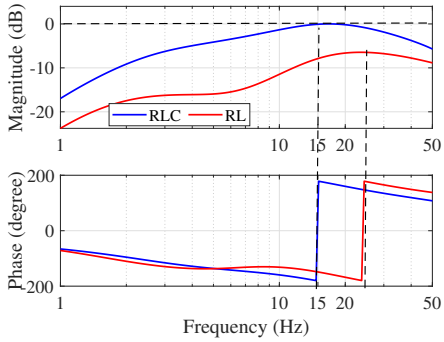

(b)

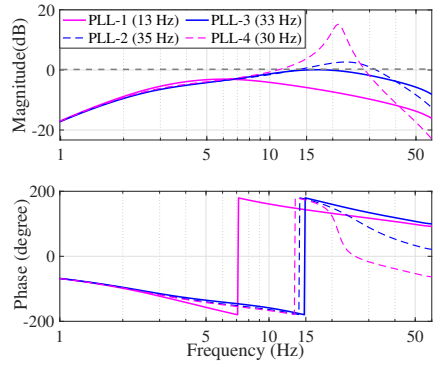

(c)

Fig. 10: Frequency-domain responses. (a) GFL Block-1. (b) G_{OL}. The red curve is the response with the RL network, and the blue curve is with the RLC network. The effective grid reactance is 0.34 pu for both the RLC and RC circuits. (c) G_{OL} for different PLLs. The system is connected to RLC networ, with effective impedance of 0.34 pu.

for the same series compensation level. The results showcase that PLL-4 (32 Hz) has the worst performance, while PLL-1 (13 Hz) is stable for the same level of series compensation. This analysis aligns with the information provided in Fig. 10c. For instance, PLL-1 adds a relatively less gain in the low frequency range, where has PLL-4 presents a high gain at the resonant frequency, introducing instability. This analysis also algins with the EMT simulation results presented in Fig. 3b.

For the GFM-IBR testbed, the Bode diagram of block-1 (shown in Fig. 11a) indicates a more significant gain and phase lag for an RLC network compared to an RL network in the range of 1-10 Hz for the same effective grid reactance of 0.6 pu. For the total loop gain, including the droop control, the phase shift occurs at around 6 Hz. At this frequency, when

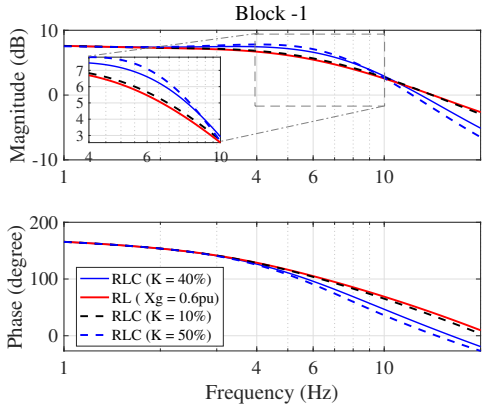

(a)

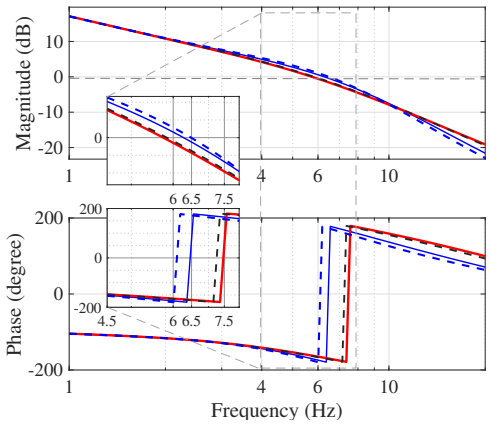

(b)

Fig. 11: Frequency-domain responses. (a) GFM Block-1. (b) G_{OL}. The red curve is the response with the RL network, and the blue curve is with the RLC network. The effective grid reactance is 0.6 pu.

the compensation level exceeds 40%, the system is unstable since the gain is more than 0 dB, while for the RL network, the system exhibits stability, as shown in Fig. 11b.

Observations made using the frequency-domain analysis align with the EMT results shown in Fig. 4b and the eigenvalue analysis results in Figs 6b and 7b.

Furthermore, decreasing the value of droop coefficient R, improves the stability of the system. Frequency domain responses of the open loop gain (G_{OL}) presented in Fig. 12a showcase, as R is reduced, the gain of the open loop is reduced at the frequency where phase shifting occurs. This is further supported by the time-domain simulation results presented in Fig. 12b. Reducing the droop coefficient from 0.05 to 0.04 enhances the system stability, leading to improved damping of oscillations.

Remarks: Based on the frequency responses of the subsystem relating the PCC bus voltage angle or real power to the synchronizing angle, the following remarks are made.

- Series compensation increases the sensitivity of the PCC bus voltage angle towards the synchronizing angle, thereby leading the GFL-IBR system more prone to instability. Reducing the PLL's bandwidth or resonance peak can help stability.
- Series compensation introduces more phase lag from

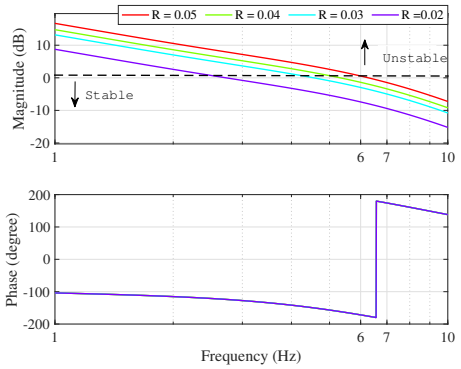

(a)

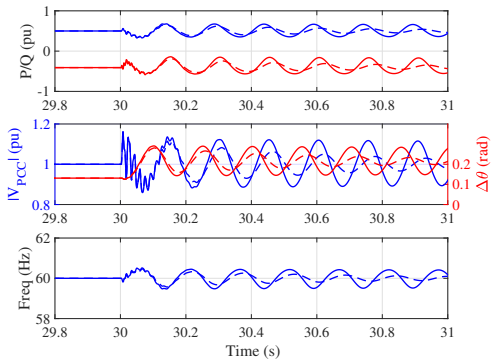

(b)

Fig. 12: (a) Frequency-domain responses. G_{OL}, when the droop coefficient (R) is varied. The effective grid reactance is 0.6 pu. (b) Time-domain responses for the real power P, Q, $|V_{\text{PCC}}|$, $\Delta\theta$, and frequency(Hz). Solid lines represents the response when R = 0.05. Dashed lines: R is 0.04.

the synchronizing angle to the real power measurement, thereby leading the GFM-IBR system more prone to instability. Reducing the P-f droop coefficient can help stability.

V. Discussion

A. GFL with f-P droop

The effect of frequency support control is examined for the GFL-IBR when it radially connects to an RLC circuit. Here, additional droop control is added to generate the P_{ref} for the outer loop, shown in Fig. 13. The frequency measurement from the PLL is compared with the nominal frequency. Their error is amplified by $1/R$ times to produce the reference power. This additional controller adjusts the power order based on frequency deviations, thereby enhancing grid-connected operations. This approach is adopted from the RECP_A WECC wind model [23]. Furthermore, the IEEE standard-2800, recommends IBRs have some frequency support capability for interconnection to the grid [24].

The time-domain simulation results showing the comparison of GFL-IBR with and without droop control are shown in Fig. 14. The RLC circuit has a compensation level of 62%. Observation from the time-domain plots shows that with the introduction of f–P droop, the system is more stable compared to a GFL-IBR without the droop control. The frequency-domain analysis can further explain the effect of droop control.

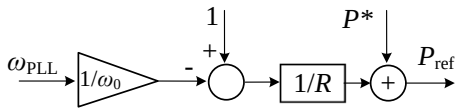

Fig. 13: Control block diagram of $f-P$ droop adopted for GFL IBR.

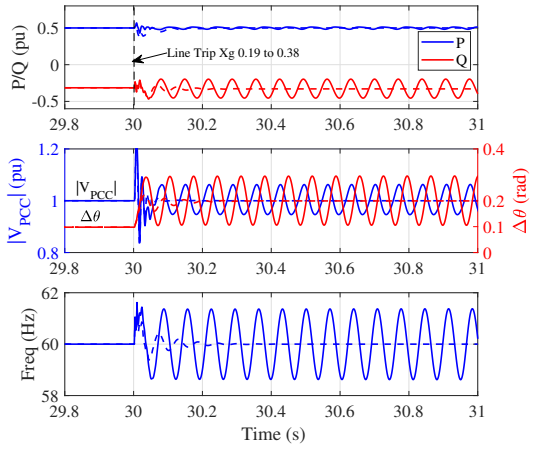

Fig. 14: Comparison of GFL with and without droop control during the series compensated network. Time-domain responses for the real power P, Q, $|V_{\text{PCC}}|$, $\Delta\theta$, and frequency(Hz). Solid lines: no droop. Dashed line: with droop. At $t = 30$ s, a line tripping event occurs leaving the IBR radially connected to the RLC network. The effective grid reactance goes from 0.19 pu to 0.38 pu.

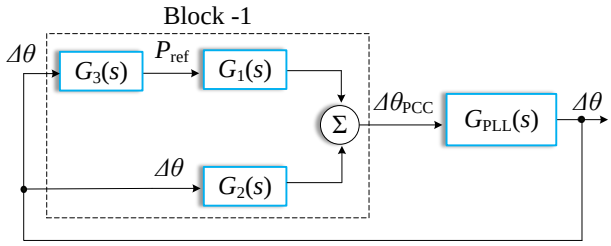

Fig. 15: Feedback construction for frequency-domain analysis of GFL-IBR with additional droop control.

The block diagram for GFL-IBR with f–P droop is illustrated in Fig. 15. In this diagram, "Block-1" is defined using three transfer functions: $G_1(s)$, $G_2(s)$, and $G_3(s)$, where $G_3(s)$ represents the droop transfer function $-s/(\omega_0 \times R)$, and $G_2(s)$ is the transfer function from P_{ref} to $\Delta\theta_{\text{PCC}}$.

Without the frequency droop control, the net transfer function for "Block-1" is $G_1(s)$. With droop, the transfer function becomes $G_1(s) + G_2(s) \times G_3(s)$. This additional path results in a reduction of the gain of "Block-1" in the frequency range of 1-30 Hz. This reduction is evident from the Bode diagram depicted in Fig. 16a.

This addition provides additional stability. The Bode diagram of the total loop gain for a compensation level of 63% is presented in Fig. 16b, where the phase shift occurs at around 15 Hz. At this frequency, GFL without droop control is marginally stable, whereas, with droop control, it indicates stability. This observation coincides with the EMT simulation

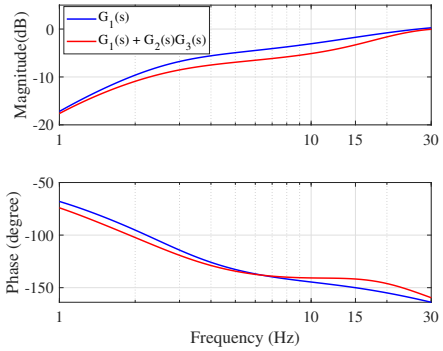

(a)

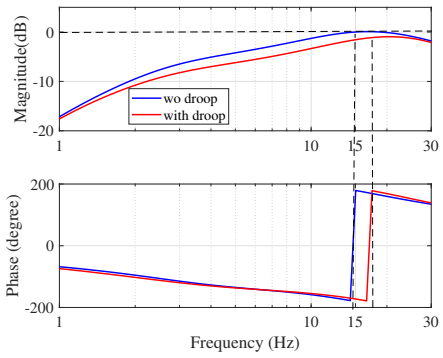

(b)

Fig. 16: Frequency domain responses. (a) GFL Block-1. (b) G_{OL}. The red curve represents the response of the system with additional droop control, whereas the blue curve is without droop control. The series compensation level is 63%.

results in Fig. 14.

Remarks: The addition of f–P droop in a GFL-IBR can help reduce the sensitivity of the PCC bus voltage angle towards the synchronization angle, thereby mitigating the interaction of series compensation and PLL and enhancing stability.

B. GFM with VSG control

An alternative control method to synchronize the GFM to the grid is explored: the Virtual Synchronous Generator (VSG) control. VSG control is a widely adopted control mechanism for the synchronization of GFM-based IBR to the grid. The synchronizing mechanism is similar to that of a synchronous generator and it power-angle relationship is determined by the second-order swing equation [25], [26]. The control implementation block diagram is provided in Fig. 17. Here, D_p is the damping coefficient of the active power loop, and J is the inertia constant. The transfer function of the VSG controller from the net power $P_{\text{ref}} - P$ to the synchronizing angle $\Delta\theta$ is given by:

$$G_{\text{VSG}}(s) = \frac{1}{Js + D_p} \times \frac{\omega_0}{s} \tag{13}$$

For the VSG controller, J is considered as 0.02 pu, and the damping coefficient D_p value is 20. The steady-state gain of frequency vs. power is $1/D_p$ in VSG and R in a P-f droop control. Therefore,

The time domain results that showcase the performance of the VSG-based GFM are presented in Fig. 18a, when the line is tripped at $t = 30$ s, the grid reactance changes from 0.19 pu to 0.38 pu. As observed in Fig. 18a, under similar operating conditions, when the VSG based GFM is connected to the RLC network, undamped 5 Hz oscillations appear, while the system is stable when connected to RL network.

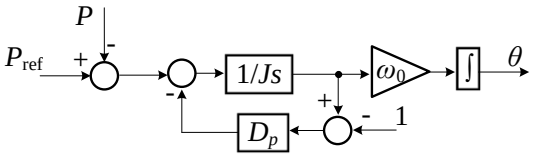

Fig. 17: Control block diagram of VSG controller adopted for GFM IBR.

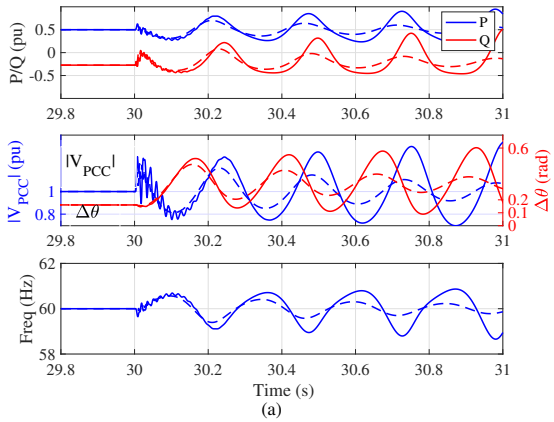

(a)

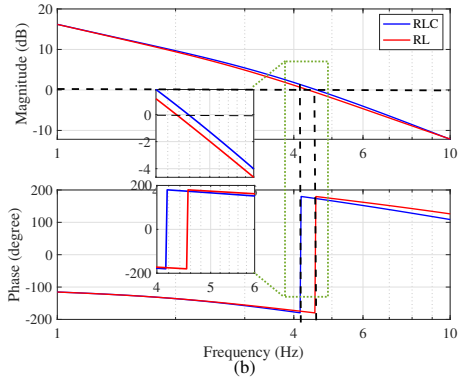

(b)

Fig. 18: (a) Time domain responses for the real power P, Q, $|V_{\text{PCC}}|$, $\Delta\theta$, and frequency(Hz) for VSG based GFM. Solid lines: RLC network; Dashed line: RL network. The system is radially connected to the RLC network at $t = 30$ s, where grid reactance goes from 0.317 pu to 0.635 pu. (b) Frequency-domain response of the open-loop gain G_{OL}. Red curve: RL Network. Blue curve: RLC Network. The series compensation level is 40%.

A similar block diagram approach, utilizing frequency domain analysis, is employed to understand the instability mechanism. The frequency response of the loop gain is illustrated in Fig. 18b. At the frequency where the phase shift occurs, the loop gain exceeds 0 dB for the system with the RLC network, indicating instability.

Furthermore, Fig. 19a shows the frequency-domain response of the loop gain as the inertia constant J varies from 0.02 pu to 0.4 pu, with D_p held constant. The results indicate that increasing J does not change the magnitude of the loop gain. However, more phase lag is introduced and the frequency where the phase shift occurs reduces. This pushes the system toward instability. The time-domain response is presented in Fig. 19b. The results indicate when the inertia constant used is $J = 0.04$ pu, oscillations are more severe compared to those when $J = 0.02$ pu.

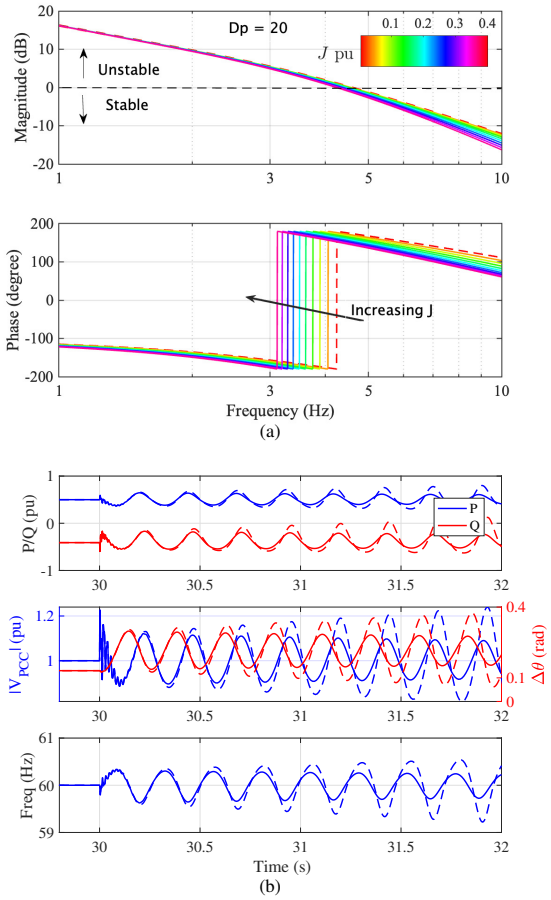

Fig. 19: (a) Frequency-domain response of the open-loop gain G_{OL} for VSG for different value of J. The series compensation level is 40%. (b) Time-domain responses for the real power P, Q, $|V_{\text{PCC}}|$, $\Delta\theta$, and frequency (Hz). Solid lines represents the response when J = 0.02 pu. Dashed lines: J is 0.04 pu.

Additionally, as shown in Fig. 20a, when J is held constant and the damping factor D_p is increased, the system's stability improves. This is further supported by the time-domain results in Fig. 20b, which demonstrate when the damping constant is increased from a value of 20 to 25, the system has a better damping performance.

VI. Conclusion

This paper investigates the interactions of series compensation with grid-connected IBRs, specifically GFL and GFM types. The study conducts EMT simulations, analytical model building, eigenvalue analysis, and open-loop frequency-domain analysis to reveal that series compensation may interact with synchronizing units in IBRs and create oscillations. Series compensation can increase the sensitivity of the PCC bus voltage angle towards the synchronizing angle, and introduce phase lag in the real power response towards the synchronizing angle. These factors may lead to interactions with PLL in the GFL-IBR systems and interactions with the power-based synchronization in the GFM-IBR systems, thereby leading to instability.

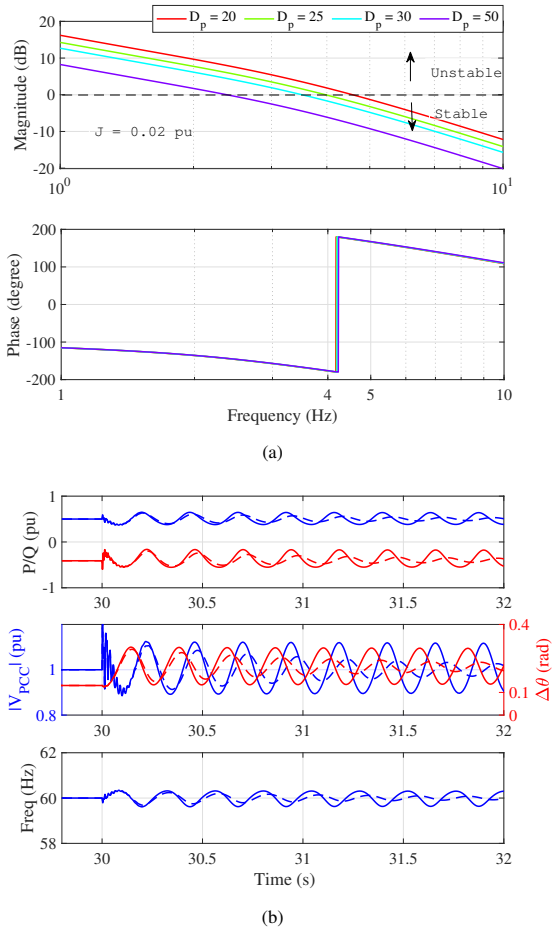

Fig. 20: (a) Frequency-domain response of the open-loop gain G_{OL} for VSG for different value of D_p. The series compensation level is 40%. (b) Time-domain responses for the real power P, Q, $|V_{\text{PCC}}|$, $\Delta\theta$, and frequency (Hz). Solid lines represents the response when D_p = 20. Dashed lines: D_p is 25.

References

[1] J. W. Ballance and S. Goldberg, "Subsynchronous resonance in series compensated transmission lines," *IEEE Transactions on Power Apparatus and Systems*, vol. PAS-92, no. 5, pp. 1649–1658, 1973.

[2] Y. Cheng, L. Fan, J. Rose, S.-H. Huang, J. Schmall, X. Wang, X. Xie, J. Shair, J. R. Ramamurthy, N. Modi, C. Li, C. Wang, S. Shah, B. Pal, Z. Miao, A. Isaacs, J. Mahseredjian, and J. Zhou, "Real-world subsynchronous oscillation events in power grids with high penetrations of inverter-based resources," *IEEE Transactions on Power Systems*, vol. 38, no. 1, pp. 316–330, 2023.

[3] L. Fan, Z. Miao, D. Ramasubramanian, and H. Ding, "Operational challenges of solar PV plus storage power plants and modeling recommendations," *IEEE Open Access Journal of Power and Energy*, vol. 10, pp. 477–489, 2023.

[4] L. Fan, R. Kavasseri, Z. L. Miao, and C. Zhu, "Modeling of DFIG-based wind farms for SSR analysis," *IEEE Transactions on Power Delivery*, vol. 25, no. 4, pp. 2073–2082, 2010.

[5] Z. Miao, "Impedance-model-based SSR analysis for type 3 wind generator and series-compensated network," *IEEE Transactions on Energy Conversion*, vol. 27, no. 4, pp. 984–991, 2012.
[6] L. Fan and Z. Miao, "Nyquist-stability-criterion-based SSR explanation for type-3 wind generators," *IEEE Transactions on Energy Conversion*, vol. 27, no. 3, pp. 807–809, 2012.
[7] X. Xie, X. Zhang, H. Liu, H. Liu, Y. Li, and C. Zhang, "Characteristic analysis of subsynchronous resonance in practical wind farms connected to series-compensated transmissions," *IEEE Transactions on Energy Conversion*, vol. 32, no. 3, pp. 1117–1126, 2017.
[8] R. K. Varma, S. Auddy, and Y. Semsedini, "Mitigation of subsynchronous resonance in a series-compensated wind farm using FACTS controllers," *IEEE Transactions on Power Delivery*, vol. 23, no. 3, pp. 1645–1654, 2008.
[9] L. Fan and Z. Miao, "Analytical model building for type-3 wind farm subsynchronous oscillation analysis," *Electric Power Systems Research*, vol. 201, p. 107566, 2021. [Online]. Available: https://www.sciencedirect.com/science/article/pii/S0378779621005472
[10] H. Ma, P. Brogan, K. Jensen, and R. Nelson, "Sub-synchronous control interaction studies between full-converter wind turbines and series-compensated ac transmission lines," in *2012 IEEE Power and Energy Society General Meeting*. IEEE, 2012, pp. 1–5.
[11] M. Beza and M. Bongiorno, "On the risk for subsynchronous control interaction in type 4 based wind farms," *IEEE Transactions on Sustainable Energy*, vol. 10, no. 3, pp. 1410–1418, 2019.
[12] Y. Xu, M. Zhang, L. Fan, and Z. Miao, "Small-signal stability analysis of type-4 wind in series-compensated networks," *IEEE Transactions on Energy Conversion*, vol. 35, no. 1, pp. 529–538, 2020.
[13] North American Electric Reliability Corporation, "Grid forming technology: Bulk power system reliability considerations," https://www.nerc.com/comm/RSTC_Reliability_Guidelines/White_Paper_Grid_Forming_Technology.pdf#search=Grid%20Forming%20Technology, [Accessed 14-01-2024].
[14] G. Li, Y. Chen, A. Luo, Z. He, H. Wang, Z. Zhu, W. Wu, and L. Zhou, "Analysis and mitigation of subsynchronous resonance in series-compensated grid-connected system controlled by a virtual synchronous generator," *IEEE Transactions on Power Electronics*, vol. 35, no. 10, pp. 11 096–11 107, 2020.
[15] G. Li, F. Ma, C. Wu, M. Li, J. M. Guerrero, and M.-C. Wong, "A generalized harmonic compensation control strategy for mitigating subsynchronous oscillation in synchronverter based wind farm connected to series compensated transmission line," *IEEE Transactions on Power Systems*, vol. 38, no. 3, pp. 2610–2620, 2022.
[16] L. Fan and Z. Miao, *Modeling and Stability Analysis of Inverter-Based Resources*. CRC Press, 2023.
[17] L. Bao, L. Fan, Z. Miao, and Z. Wang, "Hardware demonstration of weak grid oscillations in grid-following converters," in *2021 North American Power Symposium (NAPS)*. IEEE, 2021, pp. 01–06.
[18] L. Fan, Z. Wang, and Z. Miao, "Large angle deviation in grid-following IBRs upon grid voltage dip," *IEEE Transactions on Energy Conversion*, 2023.
[19] H. Ding, R. Kar, Z. Miao, and L. Fan, "A novel design for switchable grid-following and grid-forming control," *IEEE Transactions on Sustainable Energy*, 2024.
[20] L. Fan, "Modeling type-4 wind in weak grids," *IEEE Transactions on Sustainable Energy*, vol. 10, no. 2, pp. 853–864, 2018.
[21] Y. Li, Y. Gu, and T. C. Green, "Revisiting grid-forming and grid-following inverters: A duality theory," *IEEE Transactions on Power Systems*, vol. 37, no. 6, pp. 4541–4554, 2022.
[22] L. Fan, C. Zhu, Z. Miao, and M. Hu, "Modal analysis of a DFIG-based wind farm interfaced with a series compensated network," *IEEE Transactions on Energy Conversion*, vol. 26, no. 4, pp. 1010–1020, 2011.
[23] "Type 3 - Generic Wind Turbine Generator Model (Phase II) - ESIG — esig.energy," https://www.esig.energy/wiki-main-page/type-3-generic-wind-turbine-generator-model-phase-ii/#Plant_level_control_model_.28repc_a.29, [Accessed 21-02-2025].
[24] "Ieee standard for interconnection and interoperability of inverter-based resources (ibrs) interconnecting with associated transmission electric power systems," *IEEE Std 2800-2022*, pp. 1–180, 2022.
[25] H.-P. Beck and R. Hesse, "Virtual synchronous machine," *2007 9th International Conference on Electrical Power Quality and Utilisation*, pp. 1–6, 2007. [Online]. Available: https://api.semanticscholar.org/CorpusID:42096573
[26] N. Mohammed, H. H. Alhelou, and B. Bahrani, *Grid-Forming Power Inverters: Control and Applications*. CRC Press, 2023.

Ratik Mittal (Member, IEEE) received the B.E. degree in Electrical Engineering from Thapar University, Patiala, Punjab, in 2015, and the M.S. and Ph.D. degrees in Electrical Engineering from the University of South Florida, Tampa, Florida, in 2019 and 2024, respectively. He is currently an Engineer III conducting technical studies in the Transmission and Regulatory division at Quanta Technology, LLC. His research interests include modeling and analysis of power electronics-based power systems.

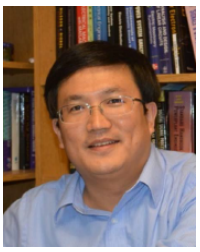

Zhixin Miao (Senior Member, IEEE) received the B.S. degree in electrical engineering from Huazhong University of Science and Technology, Wuhan, China, in 1992, the M.S. degree in electrical engineering from the Graduate School of Nanjing Automation Research Institute, Nanjing, China in 1997, and the Ph.D. degree in electrical engineering from West Virginia University, Morgantown, in 2002.

He is currently with the University of South Florida (USF), Tampa. Prior to joining USF in 2009, he worked in the Transmission Asset Management Department at Midwest ISO, St. Paul, MN, from 2002 to 2009. His research interests include power system stability, microgrids, and renewable energy. Dr. Miao aso serves as an Associate Editor for the *IEEE transactions on Sustainable Energy*.

Lingling Fan (Fellow, IEEE) received her B.S. and M.S. degrees in electrical engineering from Southeast University, Nanjing, China, in 1994 and 1997, respectively, and her Ph.D. degree in electrical engineering from West Virginia University, Morgantown, in 2001. She is currently a full professor with the University of South Florida inTampa Florida, where she has been since 2009. She was a Senior Engineer in the Transmission Asset Management Department at Midwest ISO in St. Paul, MN, from 2001 to 2007, and an Assistant Professor at North Dakota State University in Fargo from 2007 to 2009. Her research interests include power systems and power electronics. Dr. Fan served as Editor-in-Chief of *IEEE Electrification Magazine* from 2020 to 2024. She received the recipient of the 2024 Energy Systems Integration Group (ESIG) Excellent Award and the 2025 IEEE PES Wanda Reder Pioneer in Power Award.

Deepak Ramasubramanian (Senior Member, IEEE) received the M.Tech. degree from the Indian Institute of Technology Delhi, New Delhi, India, in 2013, and the Ph.D. degree from Arizona State University, Tempe, AZ, USA, in 2017. He is currently a Technical Leader at the Grid Operations and Planning Group, Electric Power Research Institute (EPRI) and leads research projects related to modeling of inverter-based resources for bulk power system analysis.